A Large Scale Analysis of the Hot-Onset Phenomenon of Solar Flares using Soft X-rays

2393774

April 2023

Abstract

Solar flares are complex and dynamic phenomena that have captured the attention of physicists for decades, as they provide an opportunity to probe the plasma dynamics and magnetic processes that govern the behavior of the Sun. The widely accepted standard flare model (Fletcher et al. 2011) predicts that hard X-rays (HXRs) produced from non-thermal electron interactions are released before soft X-rays (SXRs) from thermal electron interactions during solar flares. A recent study by Hudson et al. (2021) identifies a faint release of SXR emission at thermal temperatures (10-15 MK) before the release of any HXRs, breaking the widely accepted flare model. This phenomenon - called the 'hot-onset' - was confirmed for a set of just four flares using SXR measurements from the Geostationary Operational Environmental Satellites (GOES). Using recently updated atomic data from CHIANTI (Dere et al. 1997; Zanna et al. 2021), properly calibrated SXR data from GOES (Zetterlund & Machol 2022), and a flare lists from the heliophysics event knowledgebase (HEK) (Hurlburt et al. 2012), we sought to confirm the hot-onset phenomenon for a population of 9,573 flares occurring between 2010 and 2020, utilising lightcurve analysis and flux ratio plasma diagnostics. Our investigations confirm the presence of these hot-onset sources across our flare sample, where 94.7% of flares experienced average temperatures exceeding 7 million Kelvin during the first one-quarter of the flare rise.

1 Introduction

1.1 Solar Flares

Solar flares are among the most violent and energetic explosions in the solar system, with an energy release of up to 10^{32} ergs (10^{25} Joules). The process begins in the Sun's convective region, where concentrated magnetic activity can produce magnetic loops which then rise through the photosphere and into the Solar corona (Archontis & Syntelis 2019). The magnetic fields allow ionised plasma to flow along them, forming large flux loops. Darker regions on the Sun's photosphere - known as Sunspots - are caused by the strong magnetic fields, and are often concentrated together in groups known as active regions (Zwaan 1985). Due to the differential rotation of the Sun, the two footprints of each loop are able to move at different velocities on the solar surface, which stretches and pulls on the flux loops. A consequence of their close proximity within active regions is that these ropes often collide, breaking the bipolarity of the magnetic field line and initiating a process called 'magnetic reconnection' (Dungey 1951). This is when the magnetic field lines rapidly reconfigure, causing the suspended plasma to be accelerated, which initiates energy release across the electromagnetic spectrum.

Our focus is solely on the X-ray portion of the electromagnetic spectrum, which we categorise into two groups: HXRs and SXRs. The production of this high energy radiation begins at the reconnection point, where the reconfiguration of the magnetic fields causes plasma to be accelerated back towards the surface. This plasma consists of both ions and electrons, however the majority of emission is caused by electrons (Brown 1971). This means that non-thermal electrons are accelerated back towards the Sun's denser chromosphere region, with speeds close to the speed of
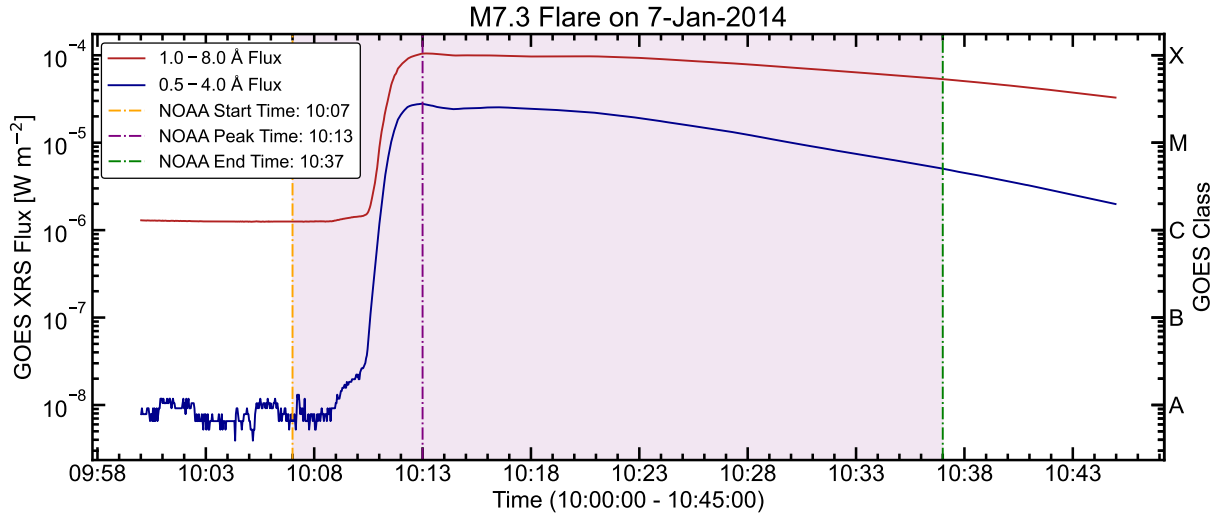
Figure 1: GOES SXR measurements of an M7.3 class solar flare occurring on the 7th of January 2014. The red line represents the XRS-B long 1‑8 Å channel flux; the blue line representing the XRS-A short 0.5‑4 Å flux. Dashed lines represent the start, peak and end times of the flare as calculated by NOAA. The purple shaded region denotes NOAA's definition of the full duration of the flare.

light. Once they enter the chromosphere, the non-thermal electrons are slowed through coulomb collisions, giving off radiation in the gamma and HXR frequencies (Lin & Hudson 1976; Brown & MacKinnon 1985). These collisional processes heat the plasma to temperatures in excess of 10 mega-Kelvin (MK), which then expands into the post-flare loops, emitting radiation in the SXR and extreme ultraviolet (EUV) range. This is the standard flare model for X-ray emission, where we emphasise that the non-thermal HXRs precede the thermal SXR emission. Proof of causality between these two emissions is given through the Neupert effect (Hudson 1991; Veronig 2003).

Solar flares are categorised into three distinct evolutionary phases, which can be seen in the GOES SXR observation of a flare on the 7th of January 2014, in figure 1. The pre-flare phase is indicated by the ambient, flat portion of SXR emission which is followed by a sharp increase of SXRs; called the impulsive phase. This reaches a peak value of flux before slowly decreasing back towards its pre-flare value, which we call the gradual phase. We note at this stage that the definition of the 'start' of the impulsive phase is ambiguous - dependent on the specific study and wavelength ranges in question - however it is largely accepted that this is indicated by the onset of HXR emission. The GOES series of satellites are used to categorise solar flares on a logarithmic scale, based on their peak flux (in [$\mathrm{Wm^{-2}}$]) detected in the 1‑8 Å channel. The definitions of these classes can be seen by looking at the right-hand y-axis of figure 1, with the highest flare classification, X-class, being for events recording a peak flux in excess of $10^{-4}\,\mathrm{Wm^{-2}}$, and so forth for M, C, B and A-class.

1.2 The Hot-Onset

The pre-flare phase of solar flares is a common place to investigate a series of phenomena called 'flare precursors', which consist of emission preceding the impulsive phase of the flare. Many flare precursors have been identified such as the 'impulsive hot footprint' phenomenon from McTiernan et al. (1993) or 'preheating' from Hoven & Hurford (1986). These precursors are conformative to the standard modelling techniques outlined in the previous section, as they are detected through the release of HXRs from non-thermal sources.

The hot-onset is a flare precursor identified by Hudson et al. (2021) over a series of four selected solar flare events using GOES SXR measurements, which finds the presence of early onset

SXR emission. They define these onsets as appearing with elevated SXR emission before any evidence of HXRs, which is in contradiction to the widely-accepted standard modelling techniques from 1-D radiation hydrodynamics in the standard framework (Nagai 1980). They derived plasma parameters from each event, concluding that that these onsets are emitting at temperatures in the 10-15 MK range but with an emission measure at low orders of magnitude. This means that these early-onset sources are hot, implying the presence of thermal electrons caused by some pre-flare heating process which is not predicted by the solar flare model.

Hudson et al. (2021) calculated background and onset intervals 'by eye' - which is not realistic for a large-scale analysis - therefore we need to develop an algorithm to determine these properties automatically. They also analysed the four onsets using HXR data acquired from the high energy channels of the Reuven Ramaty High Energy Solar Spectroscopic Imager (RHESSI) (Lin et al. 2003). This was used to confirm that the 'by eye' determination of the end of the onset interval coincides with the onset of HXR emission. Additionally, spatial data from the atmospheric imaging assembly (AIA) on board the solar dynamics observatory (SDO) was analysed to investigate the cause of this pre-flare heating. Spatial analysis of the 131 Å band concluded that the hot-onsets occurred in footprint and low-lying loop regions before becoming a part of the overall flare structure. Hudson also notes that they analysed RHESSI HXR spectra to look for the 'causal HXRs' which the Neupert effect predicts, however none were found.

1.3 Geostationary Operational Environmental Satellite

Since 1975, the GOES satellites have been continuously observing both Earth and the Sun with a suite of scientific instruments to monitor and predict both atmospheric and space weather, which are operated by the US Department of Commerce's National Oceanic and Atmospheric Administration (NOAA). The X-ray Sensor (XRS) has been a feature of every satellite in the series, consisting of two solar-facing detectors which measure SXRs in different wavelength bands. XRS-A measures in the short 0.5 - 4 Å band, and the XRS-B in the and long 1 - 8 Å band; the lightcurve for a solar flare recorded by these bands can be seen in figure 1. The XRS instruments capture X-rays with a two-second time cadence and observe the full solar disk, so their raw one-dimensional fluxes contain SXR contributions from across the whole disk.

The XRSs detect X-ray flux by collimating the X-ray beam and passing towards an ion chamber, where interaction with a noble gas induces a measurable current. The two sensors are identical with the exception of the thickness of a beryllium window, and the noble gas used. These properties are used to define the wavelength operating ranges (Hanser & Sellers 1996). Raw measurements of the XRS are not in terms of flux, but instead in terms of the current induced in the ion chamber.

These currents are converted to a raw flux by dividing by the unique wavelength-averaged transfer function pertaining to each XRS. However these raw fluxes need to be corrected for electronic gain and instrumental flux variations, to ensure calculated fluxes are consistent. Flux variations caused by instrumental noise are calculated in-flight during specific calibration periods in which both XRS instruments are pointed away from the Sun. Gain variations caused by the degradation of instrument electronics over time will affect the perceived current from the ion chamber and thus the measured flux. The calculation used to provide true flux values are given by Machol et al. (2022b):

$$\phi_{\text{corrected}} = (\phi_{\text{measured}} - \phi_{\text{instrumental}}) \times \frac{G}{C}. \tag{1}$$

Where the $\phi_{\text{corrected}}$ and ϕ_{measured} denote the corrected and measured fluxes; $\phi_{\text{instrumental}}$ the instrumental background flux; G the gain factor; and C the units conversion factor.

1.4 XRS Data Products

These corrected fluxes are termed as 'operational' data. However 'science quality' data products are developed during post-processing of the operational data, which have electron noise reduction
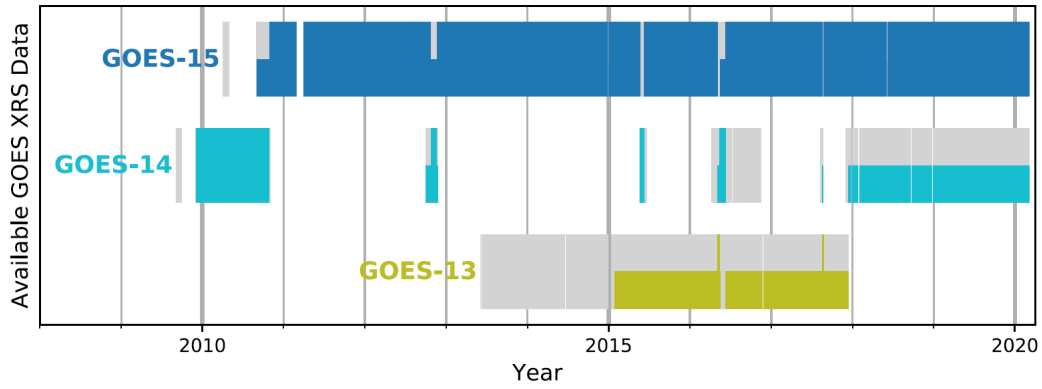
Figure 2: Science-level data availability of GOES 13-15. Full colour bars represent that the satellite was set as the primary; half colour bars for the secondary. Grey regions represent science-level data is available. Taken from Zetterlund & Machol (2022).

and a series of data flags applied (Zetterlund & Machol 2022; Machol et al. 2022a).

The electron contamination reduction is performed using a non-negative least-squares fit of the one-minute irradiance product from the 'Energetic Proton, Electron and Alpha Detectors' (EPEAD) instrument on board the GOES satellites (Rodriguez 2014; Bruno 2017). Due to the higher time cadence, these reductions are not as accurate for our two-second data, which leads to the possibility of inaccuracies - especially in the nosier short channel. The science level data contains a set of flags to further reduce 'bad data'. These include eclipses from Earth, Moon or unknown objects; calibration flags; data spikes from cosmic rays; saturated data; and temperature recovery flags. The temperature recovery flag is implemented because during an eclipse or calibration, the temperature of the instrument will cool, so needs time to get back up to an constant operating temperature in which the measurements will be consistent and reliable.

The science quality data for short-cadence measurements is only available for GOES 13-15, which had highly overlapping coverage spanning from 2009 to 2020. The exact coverage is shown in figure 2, where we can see that the longest and most consistent operational coverage is from GOES-15 (a consequence of various issues pertaining to GOES-13 and 14). We therefore chose to use GOES-15 data for our analysis as it covers the longest time range, over a full solar cycle, with consistent science-level data available.

1.5 Temperature and Emission Measure

The temperature and emission measure of the flare can be derived from the ratio of the fluxes of two X-ray channels, under the assumption that the flaring plasma in the GOES passbands is isothermal (Thomas et al. 1985). We can produce a temperature response function from the convolution of the wavelength-dependent instrument response function, and the temperature and wavelength-dependent solar response function. This gives us a temperature response in $[\mathrm{Wm}^{-2}\mathrm{cm}^3]$ at the isothermal temperature $[\mathrm{K}]$ for each of the XRS detectors, which is seen in the top right-hand plot in figure 3.

1.5.1 Instrument Response Function

The instrument response function is unique to each GOES XRS and it shows the sensitivity of each XRS detector to different wavelengths, shown in the left panels of figure 3. The responses are derived from a standardised calibration performed before the satellite was launched. This was conducted using an Fe-55 X-ray source (corrected to its 2.7 year half life) which determined the current response in Ampere-metre-squared per Watt ($\frac{\mathrm{Am}^2}{\mathrm{W}}$), which was then combined with theoretical wavelength-dependent responses to produce the final function. Despite the ion-chamber
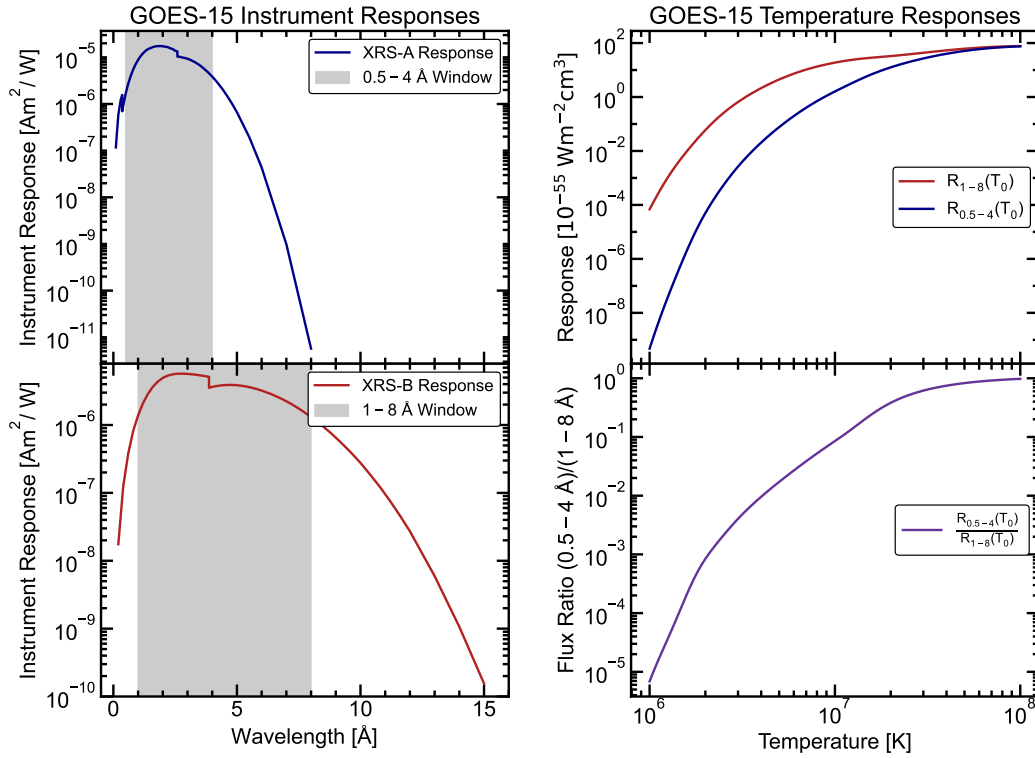
Figure 3: Left panels: The instrument response functions for the XRS-A and XRS-B channel, highlighting the intended operating windows of the two detectors in grey. The sharp drops in response seen here are caused by the Xe L-shell absolute edge and the Ar K-shell absolute edge, for the short and long channels respectively. Top right panel: temperature responses for XRS-A (blue) and XRS-B (red). Bottom right panel: the ratio of the short and long channel temperature responses.

designs being identical from GOES 8-15 (Hanser & Sellers 1996), each XRS has a different instrument response caused by tolerances allowed during manufacturing leading to small variations in responsivity. It is therefore important to use the unique response belonging to the relevant XRS. A full description of the calculations used to determine the response functions can be found in Garcia (1994).

1.5.2 Solar Response function

A theoretical solar response is required to determine the emissivity of the solar plasma for each of our XRS wavelength ranges (0.5 - 4 Å, 1 - 8 Å). We use V10.0.1 of the CHIANTI atomic database (Dere et al. 1997; Zanna et al. 2021), which uses a mixture of theoretical models and experimental results in order to access a plethora of atomic information which is used heavily in the field of solar physics. This includes calculation of ionisation equilibria, as well as continuum from free-free, free-bound and two-photon processes in order to determine both atomic line and continuum components of the solar spectrum. The spectra are calculated with a high spectral resolution of 0.01 Å with an assumed density of 10^{10} cm^{-3}. A study by White et al. (2005) compared responses of different density assumptions (both 10^9 and 10^{11} cm^{-3}) and 'no significant differences' were found. We can calculate the spectra for a range of temperatures, spaced logarithmically between 1 and 100;,MK, in order to create a response function in terms of wavelength and temperature.

The theoretical solar response can be determined using one of two assumptions of the atomic abundances of the flaring plasma: photospheric and coronal. We will be looking at the case of coronal abundances as they are dominated by a free-bound emission in the 3-6 Å wavelength range. This has the implication of giving a much higher continuum level (than the photospheric assumption) that peaks at shorter wavelengths at temperatures above 10 MK (White et al. 2005), resulting in

the short channel flux to increase much higher.

1.5.3 Flux Ratio Diagnostic

This technique was developed by Thomas et al. (1985), and then improved by Garcia (1994) for the specific use on GOES satellite data. The underlying assumption of this diagnostic technique is to assume the emitting plasma is isothermal, which means that the temperature of the plasma that is contributing to the SXR emission in any wavelength range from any plasma component is the same. Therefore the measured isothermal temperature will be the measure from the plasma which dominates the emission. Assuming this isothermal emission, the observed flux is equal to the multiplication of the emission measure, EM_0, and the temperature response function, R, at the arbitrary isothermal temperature, T_0,

$$\phi = EM_0 \cdot R(T_0). \tag{2}$$

However we do not know EM_0 or T_0 at this point, so we cannot recover either. We do however see that

$$\phi \propto R(T_0), \tag{3}$$

which allows us to eliminate the constant EM_0. By taking a ratio of fluxes of the two wavelength channels, for which we know F and R for each, we can form the equation:

$$\frac{\phi_{0.5-4}}{\phi_{1-8}} = \frac{R_{0.5-4}(T_0)}{R_{1-8}(T_0)}. \tag{4}$$

The response ratio on the right-hand side of the equation can be calculated by taking the ratio of the responses, and interpolating over a range of flux ratios and temperatures, shown in the lower-right hand plot of figure 3. We should note here that this ratio response is very sensitive in the 10-15 MK range of temperatures that was reported as the onset temperature range by Hudson et al. (2021). From the interpolated ratio response we can recover the isothermal temperature T_0. We then use the value for T_0 to calculate the emission measure by rearranging equation 2, and using our values from the long 1 - 8 Å channel for the flux and temperature response,

$$EM_0 = \frac{\phi_{1-8}}{R_{1-8}(T_0)}. \tag{5}$$

We can repeat this calculation for each flux bin, which is every 2 seconds on GOES-15, in order to create time-dependent plots for flux, temperature and emission measure as seen in the top-left 'no subtraction' panels of figure 4.

1.6 Flare Lists

The GOES satellites provide us with SXR data, however the data products do not notify us of flare occurrences. Flare identification is perfromed using an algorithm that is deployed by NOAA to compile the 'GOES flare list' of solar flare events. The algorithm that is used to identify the flares (Machol et al. 2022a) uses the 1-minute average data product, and identifies flares as 'four consecutive bins that all have a flux above a B1.0 level, where the fourth bin increases in flux by 1.4 times that of the first'. The start time for this event is set to the first of those four bins, the peak time as the point of maximum flux following the start, and the end time the point in which the maximum flux has halved.

Looking at figure 5, we can see all of the identified flares from the GOES flare list highlighted by the coloured bands. We notice that not all the flares have been flagged up by this algorithm, indicating that it is not completely reliable (many undetected spikes). We also cannot rely on the accuracy of these timings, as they use one-minute averaged data, and lax definitions - which offer poor indication of the precise start and end times. However, we can still use these NOAA timings for
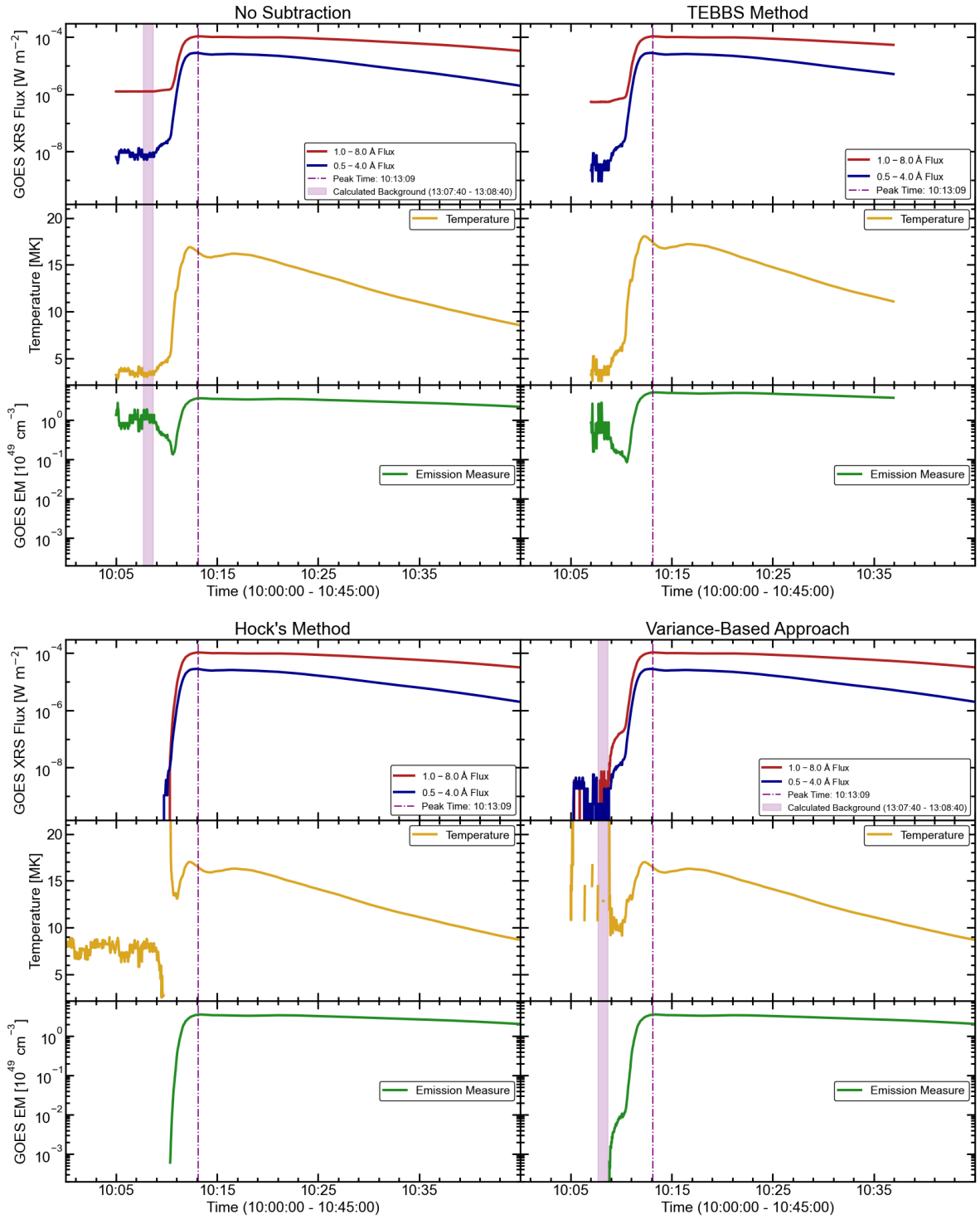
Figure 4: SXR flux, temperature and emission measure time-series data for the M7.3 flare occurring on the 7th of January 2014. Top-left panel: raw SXR flux contributions from the whole solar disk and the derived temperature and emission measures from these. Top-right panel: background subtracted fluxes using the TEBBS method Ryan et al. (2012), which is not sensitive to the low flux values. Bottom-left panel: background subtracted fluxes from Hock's method, which does not accurately isolate the flaring component due to too broad a definition of the background interval calculation. Bottom-right panel: background subtracted fluxes from the proposed variance-based approach, which accurately isolates the faint hot-onset component - even at the faintest fluxes. Pink highlighted regions denote the background subtraction interval of the variance-based approach, and dotted lines show the peak of the flare from the maximum value of long channel flux.
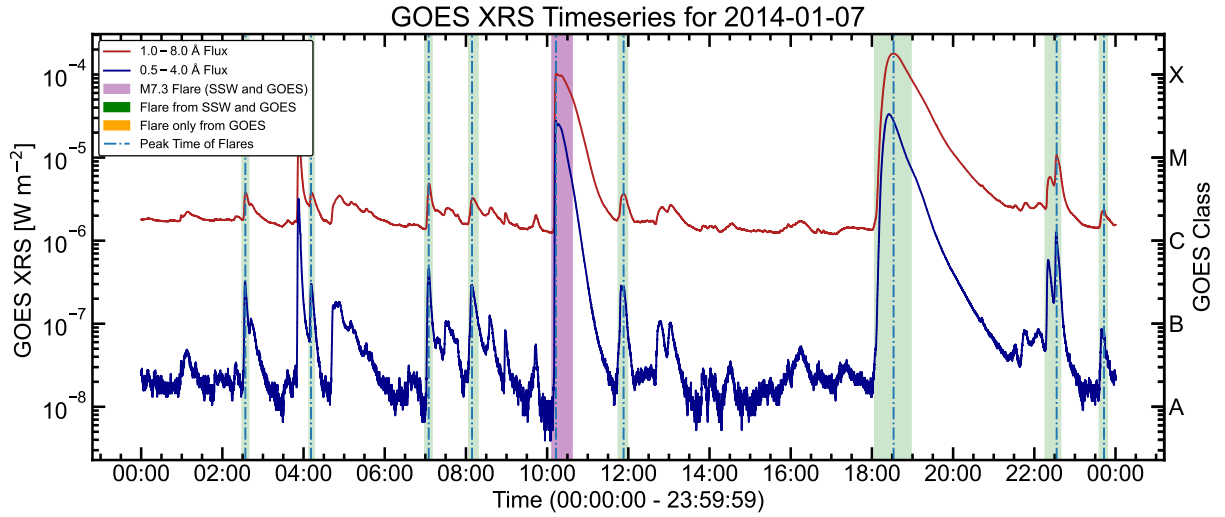
Figure 5: A full-day set of measurements from both XRS detectors from the GOES-15 satellite on the 7th January 2014. Highlighted regions denote the start and end times of flares, as calculated by NOAA. Dotted lines indicate the peak of the flare in the XRS-B long channel. The purple highlighted region is of the M7.3 flare displayed in figure 1; the green regions are flare events available from both the SSW latest events and GOES flare lists.

indication of the rough epoch of a given flare. We can query the 'heliophysics event knowledgebase' (HEK) (Hurlburt et al. 2012) to access the 'GOES' flare list, which calculates the flare timings as outlined above. We can also query other flare lists such as 'solarsoftware (SSW) latest events', which uses image data from the AIA/SDO to calculate difference images which can infer a flare location. We use a combination of both the GOES and SSW latest events list since due to missing data values from SSW; so that GOES fills in the gaps.

2   Procedure

There were two main problems that needed to be overcome before being able to calculate an average temperature and emission measure over the onset interval of a solar flare. The first is to calculate an accurate background in order to isolate the flaring component of the SXR emission. The second is to then identify the onset interval, the period that precedes HXR emission at high temperatures. Once these have been found, we can go on to calculate a weighted-mean of the flux for each background-subtracted channel over the period of the defined onset.

2.1   Background Subtraction

The GOES XRS measurements are taken of the 'Sun as a star'. This means that the detected X-rays are contributed from sources over the whole solar disk. As we are only wanting information on a particular flare, we want to isolate its contribution from the rest of the disk by performing a background subtraction. However we are also wanting to isolate the hot-onset precursor as well as the flare contribution. Hudson et al. (2021) show that the onset directly precedes the impulsive phase rise, as their spatial imaging analysis shows that the sources integrate into the overall flare structure. The most important property of the hot-onset SXR emission is that it occurs at low fluxes - much less than that of the peak of the flare - which means that it is imperative that the background is calculated as accurately as possible, such that it is sensitive to these low fluxes.

Current background-subtraction algorithms are available for use on GOES data, such as the 'Temperature and Emission measure-Based Background Subtraction' (TEBBS) method (Ryan et al. 2012) and Hock's method (Hock 2012). We will begin by discussing the effectiveness of the exist-

ing methods, before outlining a new variance-based approach which we choose for our analysis. Testing of these methods is showcased on the M7.3 flare which occurred on the 7th of January 2014, where the subtracted fluxes and derived temperature and emission measures are shown in figure 4 for each method.

2.1.1 TEBBS Method

One of the most popular methods is that of the TEBBS algorithm. The basis of this method began from work by Bornmann (1990), which developed a method that differed from a conventional linear background subtraction. They argue that subtracting off the pre-flare flux is invalid as this presumptuously assumes that there is no flare emission before the impulsive phase rise. Therefore they created an alternative method that would use derived temperature and emission measures to directly calculate the background fluxes for subtraction. Research by Ryan et al. (2012) continued the investigation into the use of temperature and emission measures, which resulted in the development of the TEBBS algorithm. They successfully applied their method to a historical catalog of 50,000 GOES-detected solar flares between 1980-2007, with the aim of classifying peak temperatures and emission measures for each flare.

However there are problems with using this method for our purposes. Firstly, their investigation was only concerned with the peak of the flare, so their algorithm is not designed to be sensitive to detecting the faint flare emissions of the hot-onset - we can see proof of this in the TEBBS column of figure 4. This shows that the TEBBS algorithm is unsuitable for our use, as it is unable to isolate the low fluxes, hence deriving very similar temperature and emission measure profiles as the no-subtraction case. We note that though it may not be suitable for our uses, the TEBBS algorithm is the most sensitive to the peak temperature over the other examples, and succeeds in what it was designed to achieve.

2.1.2 Hock's Method

Hock (2012) developed a simple background interval calculation for GOES SXR data, while using that interval for background subtractions on data from SDO/AIA. The interval was calculated by looking at a window starting at 45 minutes before the recorded NOAA start time and ending at the NOAA start time. The start point would be advanced forward to the NOAA end point of a previously-occurring flare if one was present within the 45-minute window. The minimum flux of this period would then be located, which a four-minute window would be centered around; defining a fixed four-minute background interval. The calculation of the interval within the specified window is shown in equation 6.

$$E_{bkgd} = \langle E(t_{min} - 2 \text{ minutes} : t_{min} + 2 \text{ minutes}) \rangle. \tag{6}$$

However there are notable issues with this method. Firstly, it heavily relies on the GOES flare list - and thus NOAA - to accurately define the start and end points of flares; which we know are not reliable. This method also ignores any variation in flux that could occur within the large four-minute window, since the local flux minima does not guarantee local minima in variance: a better measure of 'flatness' of a background interval. Biasing the background to the minimum flux in a 45-minute window can result in a background subtraction being not large enough, and too far in time from the event occurring - resulting in the subtraction being too weak and not being resolve the 'bump' in SXRs corresponding to the hot-onset.

Proof of these inaccuracies can be seen in the bottom-left column of figure 4, where an over-estimation in the background has resulted in the onset for both channels to be smeared out, and therefore no evidence of the onset sources from Hudson et al. (2021) can be identified. Though this method may work in some cases - however as seen in our example - it is not reliable enough.

2.1.3 Variance-Based Approach

The TEBBS method is not applicable for our uses as outlined above, so it was decided to go for a similar methodology to Hock's method - to calculate a fixed-length background interval in the pre-flare - but with the introduction of complex constraints in order to increase the accuracy. We decided to use the short channel - despite its issues with a low SNR from electron contamination - for the analysis. This is because the short channel is much more sensitive to the flux variations caused by the onset sources and it begins its exponential rise phase before or at the same time as the long channel does. This means that as long as we do not select a background interval that overlaps an increase in short channel flux, then we will not be washing out the onset contribution from either channel.

The first step is to reduce the extremities of flux variance from the short channel by re-sampling the two-second time cadence to ten-seconds. Despite losing some temporal evolution, this is necessary to make the flux values consistent, as dropouts and null values are very common. We then truncate the SXR data to a window immediately preceding the flare. We define this window by first beginning with the unreliable NOAA start time - which by its definition is always earlier than the main rise of the flare - and defining a period five minutes before this to ensure coverage of an extended pre-flare region. We truncate the data from this point until the peak of the flare.

A derivative-based approach was initially considered to locate minima and maxima of the spectrum, however the digitisation of the GOES XRS data is larger than the noise from Poisson-based photon counting statistics, as described in Simões et al. (2015). This approach was also very sensitive to fluctuations in the data. We instead looked at using a variance-based approach in order to effectively measure the gradient of the flux lightcurve without this digitisation occurring.

The variance-based approach is performed by using a one-minute sliding frame which calculates the variance of the flux from the previous 30 flux bins, for the duration of our defined window. This allows us to plot the variance over the course of our window - as shown in the bottom panel of figure 6 - which clearly shows the variance minima ('flattest' regions) in the buildup to the peak of the flare. Looking closely at figure 6, we note that the hot-onset SXR flux from the top panel also corresponds to a 'bump' in variance; something we shall return to in the following section. We then want to use one of these minima as our one-minute background interval, however we first need to decide which one to choose. We do this by constraining 'allowed' minima which are denoted by the dots in figure 6 by calculating limits for flux and variance. The minima are determined using a peak finding algorithm from SciPy (Virtanen et al. 2020), where the chosen point was taken to be the closest to the peak of the flare - highlighted in red in figure 6. Since this single point refers to the variance of a one-minute interval, we take this one minute period in the 2-second data to define our background. We use this same background interval for both the short and long channels in order to find an average flux. It is worth noting that a one-minute background interval was decided instead of a varying one, as this was short enough to give better accuracy; but long enough to give a high enough signal-to-noise ratio from its thirty-bin span. This approach biases selection to a low-variance interval of the pre-flare that immediately precedes the main rise of SXRs. Looking at the bottom-right panel of figure 4, we see that this method effectively isolates the 'bump' in SXR emission before the main SXR rise in both the long and short channels - which the other methods are not capable of. This 'bump' of SXRs corresponds to the hot-onset, where quick inspection of the temperature derived from the fluxes from this bump shows that this emission is hot - at around 10 MK - while the emission measure is low - proportional in shape to the flux bump.

2.2 Onset Interval

We know that the the SXRs from the onset directly precede the bulk emission of SXRs from the impulsive rise phase; we now seek to temporally isolate these two components. We could use the temperature and emission measure light curves to identify the onset, however doing so would introduce a bias to our results as these components are directly derived from the flux. Hudson
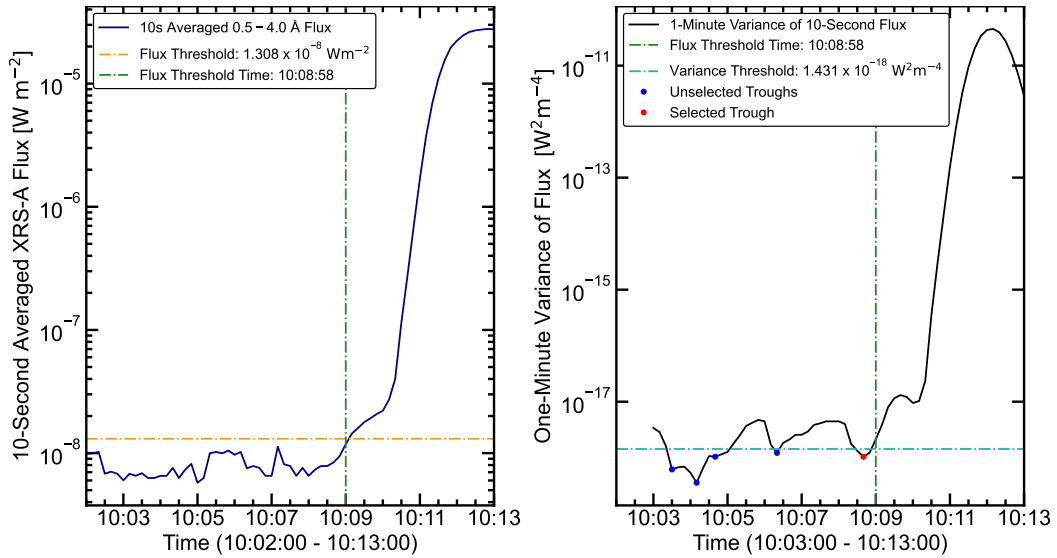
Figure 6: Left panel: The ten-second averaged short channel flux from the 'search' region. Plotted are the flux threshold calculated by the algorithm in yellow, and the corresponding point in time that this occurs at. Right panel: One-minute variance rolled over the the ten-second averaged flux. Highlighted are the time of the flux threshold, and also the value of the variance threshold calculated by the algorithm. The coloured points denote minima in the variance within the threshold region; the red point denoting the chosen point.

et al. (2021) derived these intervals 'by eye' using the background-subtracted flux curves and then confirming them by cross-referencing with HXR data obtained from the RHESSI satellite. The use of RHESSI HXR data was valid for their study as they were only analysing four flares, which were chosen partly because they had the RHESSI data available. The main issue with using RHESSI to define a 'cut-off' of the onset interval is the inconsistent solar coverage caused by its low Earth orbit; making it very prone to eclipses of Earth. This results in the RHESSI light curves experiencing sporadic data gaps - a study by Milligan & Ireland (2018) shows that it partially captured 58% of flares on the GOES flare list, however this can range anywhere from the full-flare to two seconds of coverage. Since we require a continuous data stream we cannot reliably use HXRs for our large scale analysis.

We therefore look to develop an automatic technique to 'pick out' the bumps of SXR emission in our background-subtracted SXR spectra, where we first developed a variance-based approach. This approach worked very effectively for a small number of flares, however the highly varying nature of the SXR rise phase caused too many invalid results. Since we were unable to consistently define the onset interval, we opted for a fixed interval approach to best estimate the onset interval. Despite not being able to select the exact period for each flare, we can still use it to infer the presence of the onset through the use of fractional intervals - chosen to be a fraction instead of a set time as the rise phase can highly vary in length.

Despite this fixed approach not being able to choose the exact period for each individual flare, we can still use it to infer the presence of the hot-onset through looking at fractional stages of the flux evolution until the peak of the flare, as seen in figure 7. We looked at fixed intervals of: an eighth, sixth, quarter, third, half, two thirds and three quarters of the rise phase - examples of which are shown in figure 7. The start of the rise phase was defined by the point in which the short and long channel fluxes were at sufficiently high magnitudes - around that of their pre-background subtracted level. It is imperative that we do this due to the time-delay of the long channel, which when background-subtracted using short-channel timings often results in fluxes that are effectively zero - causing skewed flux ratios and therefore artefactual temperatures.

In order to choose the most suitable interval, we looked at the small number onset intervals that
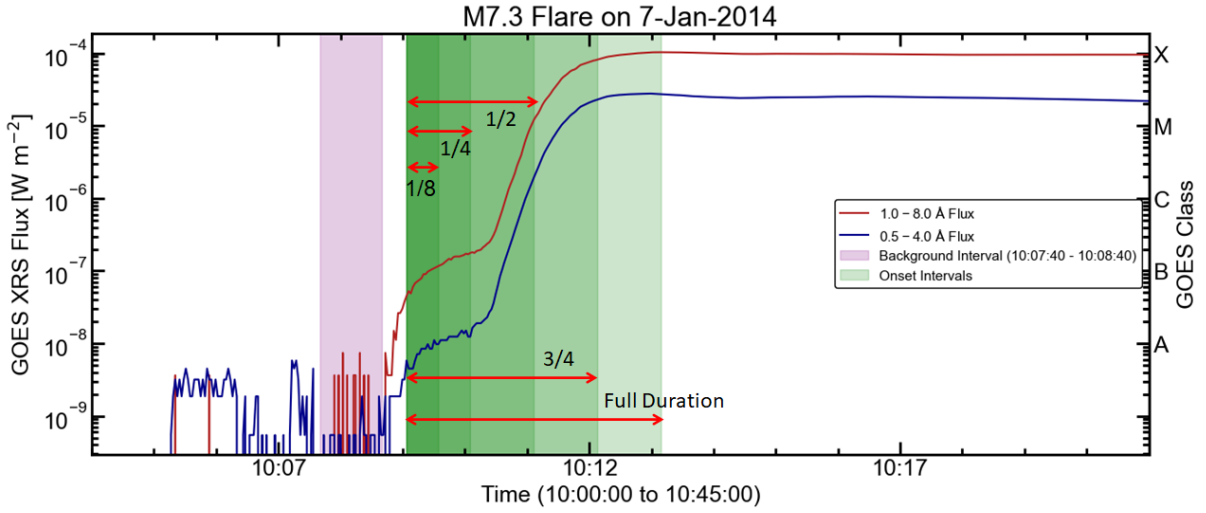
Figure 7: The background-subtracted fluxes for the M7.3 flare on the 7th of January 2014, overlaid with the fractional onset intervals shaded in green. The pink highlighted region denotes the variance-based background subtraction interval.

we successfully calculated using the variance approach - where the 1/4 interval was the best fit for these samples. To calculate the average temperature and emission measure, we calculated a mean-weighted flux over the defined one quarter interval for each channel before using our temperature and emission measure calculations to output a single value.

3 Results

Temperature and emission measures were calculated for a sample of 9,573 unique events. In order to reduce noise on the final comparisons, events where the background selection failed (454) and events which occurred within thirty minutes of another flare's NOAA end time (1,965) were removed from the sample.

3.1 Large Scale Analysis

Figure 8 displays a frequency plot of flaring temperature and emission measures for two phases of the flare. The left-hand correlation plot of emission measure and onset temperature has a roughly multivariate normal distribution, around 1.19×10^{47} cm^{-3} and 10.73 MK. The prevalence of this hot source at low emission measures is notable when compared to the right-hand panel: the temperature and emission measure at the peak of the long channel flux. In a scenario without the hot-onset phenomenon, we would expect to see much cooler temperatures at the lower emission measures due to the gradual heating of thermal electrons; an example of which is shown by the Hock and TEBBS methods in figure 4, which wipe our the hot-onset. The widespread nature of the high temperatures of these sources at low emission measures is proof that a mechanism not predicted by the standard flare model is at play. The bottom of the left-hand plot contains are a string of outliers that do not conform to the distribution. This is likely due to outlier flux values not caught by the algorithm - an inspection of the response ratio from figure 3 shows that these low temperatures are likely caused by low flux ratios which do not have as sensitive response at values below a few MK. The right-hand plot shows the peak temperature and emission measures have a strong positive correlation - consistent in the result from the TEBBS method from Ryan et al. (2012), but contradictory to a large scale study of microflares by Hannah et al. (2008).
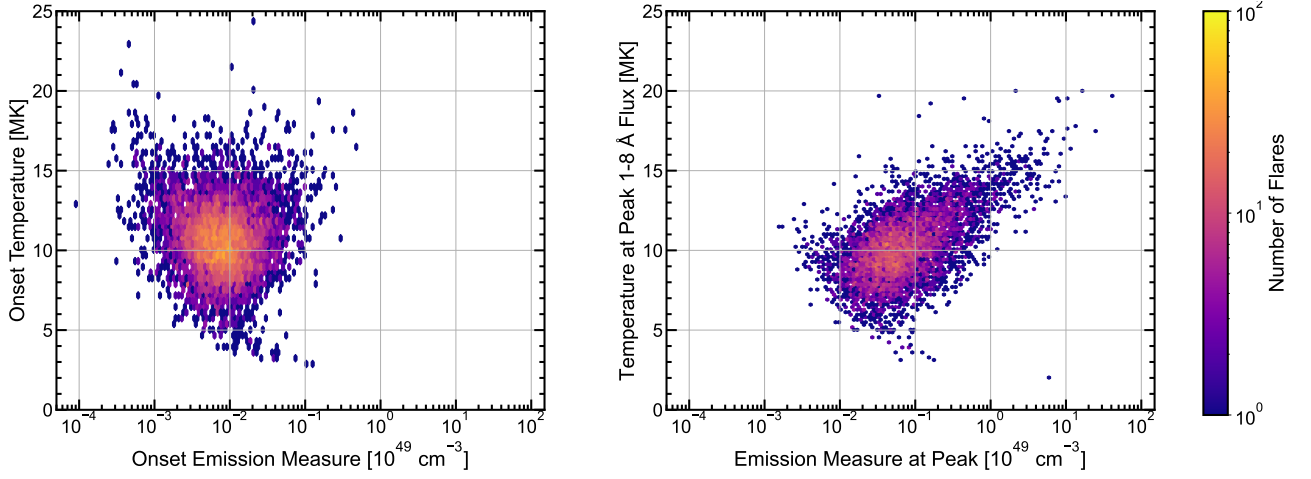
Figure 8: Left panel: the correlation between average temperature and emission measures from the hot-onset interval. Right panel: the temperature and emission measure at the peak of the flare. These are plotted as 2-D histograms with a logarithmic frequency, to highlight the concentration of flares.

3.1.1 By Flare Class

Higher peak X-ray fluxes are much less frequent than that of lower fluxes - in fact there exists a power law relationship which signifies that the vast majority of flares are of low fluxes (A or B type) (Aschwanden et al. 2021). Only 5.7% of our flare sample are X or M class, so our distributions are dominated by these lower classes and therefore lower temperatures due to the power law between peak temperature and peak flux - which was investigated by Ryan et al. (2012). We therefore split the onset temperature distribution by flare class - intrinsically meaning the peak flux - which can be seen in figure 9. It is important to distinguish that the plotted peak fluxes are from the calculation of 'new' peak fluxes using two-second cadence with the newly updated science-data; however the four panels representing X, M, C and B classes are separated using by the 'old' classification indicated by the GOES flare list from NOAA. We have done this to observe the 'migration' of flares between the class boundaries - which can also indicate noise in the sample if the migration is disproportionate.

Looking at the class breakdown plots on the right hand side of figure 9 we first observe that the number of flares detected for the X, M and C classes roughly follow the power law distribution, as expected. However, our sample does not include as many B-class flares as we expect from the power law, which is casued by the low flux limit of the XRS detectors. If we compare the distribution of temperatures of the two larger samples of flares - the C and B-class - we see a large variation in the B-class flares. This is a result of the B-class flares having magnitudes close to the low flux limit of the short channel and its dominance by electron contamination in quiet solar periods. We also note the migration of flares across some of the boundaries - caused by the difference in their 'old' classification and newly-calculated peak fluxes. There is more migration towards lower fluxes at the C to B class boundary, indicating again that these lower classes of flare are more prone to noise variations.

3.1.2 Temperature

We have shown that these sources are hot, and that the onset temperature is correlated with higher peak fluxes. In order to see how hot these sources are when compared to the rest of the flare, we correlate them to temperatures at points later on in the impulsive phase. Figure 10 shows the correlation of the onset temperature to the temperature at the peak of the flare (left-hand panel) and the maximum temperature of the flare (right-hand panel). We can see that the temperature of the onset correlates strongly with both temperatures occurring at later epochs of the flare, indicating
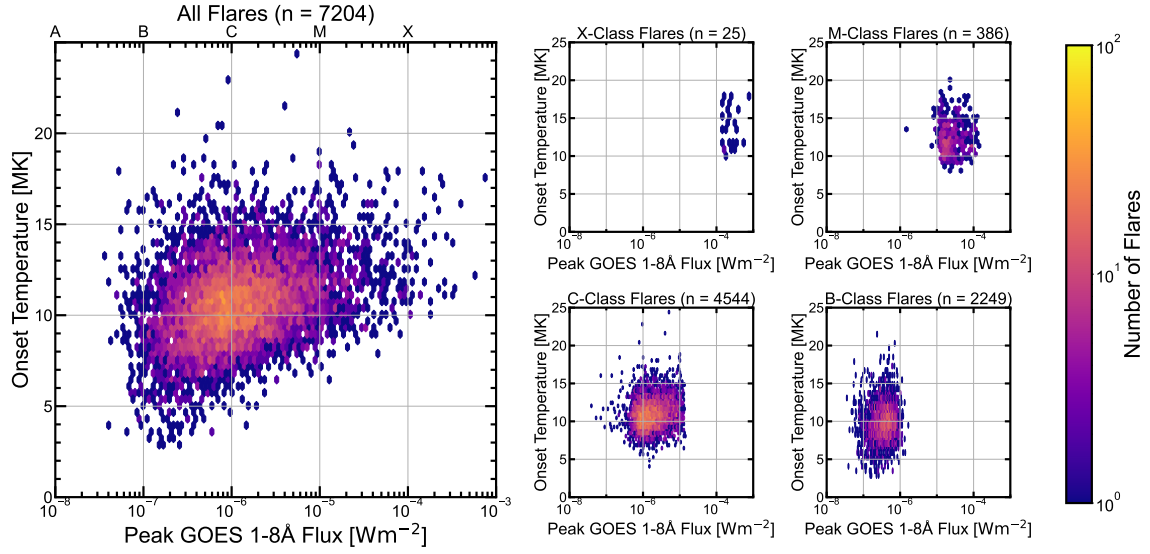
13

Figure 9: Left panel: the average temperature of the hot-onset interval, against the NOAA peak flux of the flare it is associated with. Right panels: these are then split into their respective NOAA classes: X, M, C, B for comparison. These are plotted as hexbin heat-maps in order to clearly show the distribution.
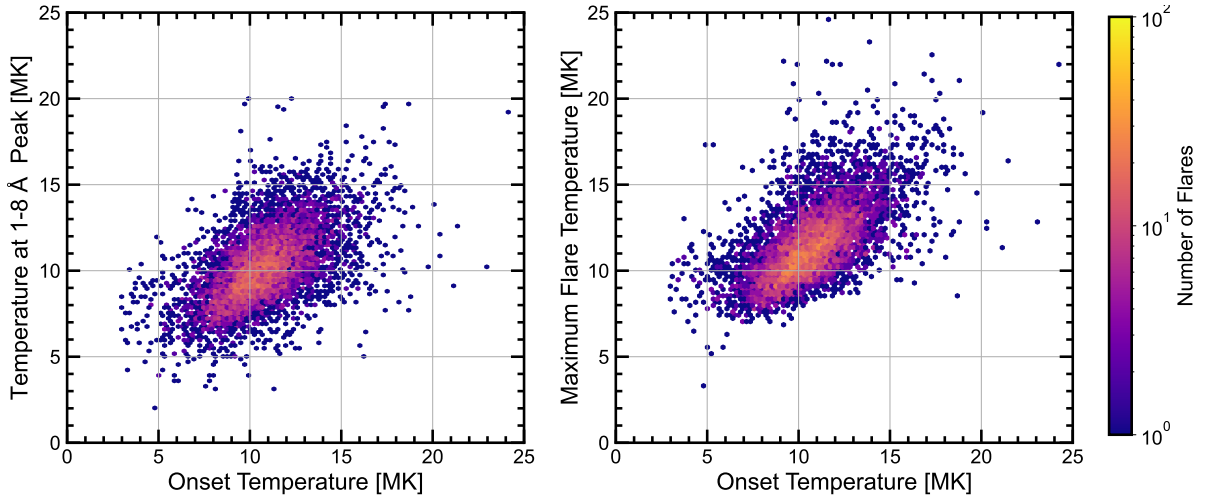

Figure 10: Left panel: correlation of the onset temperature to the temeprature at the peak of the flare. Right panel: correlation of the onset temperature to the maximum temperature of the flare. These are plotted as 2-D histograms on a logarithmic scale to show the concentration of flares.
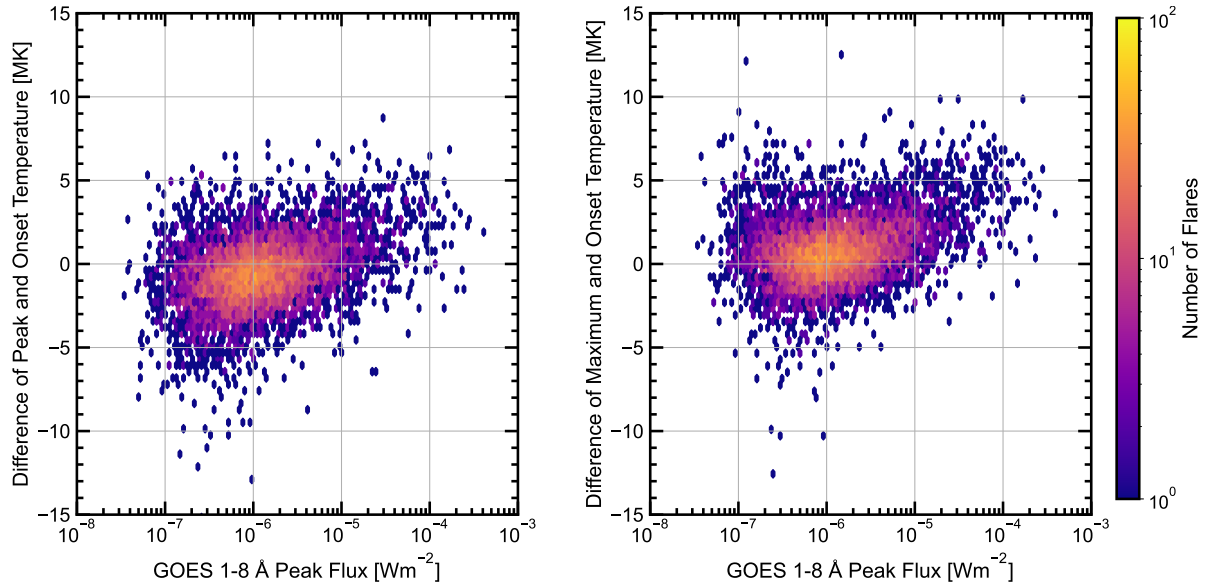
Figure 11: Relative temperature differences of the hot-onset and two stages later in the flare evolution. Left hand panel: The difference of the onset temperature and the temperature at the peak. Right-hand panel: The difference of the onset temperature and the maximum temperature of the emitting plasma.

that the heating mechanism which drives the onset temperatures is correlated to that of the known collisional heating mechanisms which drive the temperatures of the bulk SXR emission. We also observe that the maximum flare temperatures are much hotter than that at the peak of the flare, despite occurring before the peak; meaning that the bulk of the emitting plasma either cools, or becomes dominated by a cooler plasma before the peak intensity of SXR emission.

We can look more closely at the relative magnitude differences between the onset and these two later epochs of the impulsive phase, which are shown as temperature difference plots - displayed in figure 11. Looking at the left-hand panel, we can see that the majority (64%) of onsets occur at temperatures higher than at the peak of the flare - shown by the negative difference values. Looking at the right-hand panel, we can see that the majority (69%) of onsets occur below the maximum temperature. Therefore when these onsets become a part of the post-flare structures they will on average experience an increase in temperature, before falling in temperature before the peak SXR emission. This indicates that the electrons in the emitting plasma begin to cool before they reach peak emission.

3.2 Comparison with Hudson's Flares

The M7.3 flare that occurred on the 7th of January 2014 was one of the four analysed in Hudson et al. (2021), which is why it was used here as an example to visualise the automated process which we used to perform the large-scale analysis. We can directly compare the background and onset intervals for all four flares from their work, shown in table 1, where we also display our results for a comparison. For both cases the timings are derived from GOES measurements, however Hudson et al. also analysed RHESSI HXR data, finding that the HXR 'cut-off' directly aligns with their GOES onset end times in all four cases. Therefore we are also comparing our onset end times to the HXR cut-offs.

Our background subtractions are taken later in time compared to that of Hudson et al., which is due to our algorithm selecting the background as the closest possible point to the beginning of the impulsive phase rise. Despite our background interval occurring later, the most important thing to note is that there are no large overlaps between our intervals and the onset start time recorded by

Table 1: Background and onset interval timings for four flares inspected by Hudson et al. (2021), as well as our results for these events. The calculation to determine uncertainties for our temperatures are outlined in section 4.

Flare	Source	Background Interval (UT)	Onset Interval (UT)	Temperature (MK)
M1.0 2010-11-05	Hudson et al.	13:06:19-13:07:30	13:08:00-13:09:30	12.2 ± 1.1
	Our result	13:06:40-13:07:40	13:07:40-13:13:05	$9.20^{+0.53}_{-0.57}$
B9.4 2011-02-14	Hudson et al.	01:22:09-01:30:47	01:32:00-01:33:20	14.5 ± 1.7
	Our result	01:31:10-01:32:10	01:32:23-01:33:25	$14.86^{+0.58}_{-0.60}$
C1.1 2012-05-14	Hudson et al.	13:32:16-13:33:38	12:35:25-13:36:00	11.6 ± 0.9
	Our result	13:34:10-13:35:10	13:35:11-13:35:59	$8.74^{+0.95}_{-1.07}$
M7.3 2014-01-07	Hudson et al.	10:00:57-10:07:36	10:09:05-10:10:00	11.1 ± 0.6
	Our result	10:07:40-10:08:40	10:08:51-10:09:47	$9.78^{+0.61}_{-0.66}$

Hudson et al. - meaning that we are successfully biasing our background close to the flare without infringing on the SXRs released by the onset. Our use of the fixed 'one-quarter' onset interval to define the onset end agrees very well in three out of four cases. However for the M1.0 flare on the 5th of November 2010, the end of our onset interval is calculated to be much later; showing that our 'one-quarter' interval assumption does not apply to all flares. This flare was chosen by Hudson et al. to outline a 'slow and strong flare' - a flare with a slow rise and of high peak flux - so intrinsically, one quarter of this rise phase is very long. The length of this impulsive phase rise can be deemed a more extreme case, however it may point to a maximum time for which an onset may occur - perhaps indicating constraint on the unknown physical process causing the hot-onset. The temperature derived from the measurements are within rough agreement of Hudson et al. - indicating the accuracy of our methods. It is worth noting that despite the very inaccurate nature of the M1.0 flare onset interval, that the resulting temperatures are not indifferent - indicating that the temperature of the plasma during the onset is very similar to that of the rest of the flare. Although quick inspection of the temperature time series plot from the variance-based approach in figure 4 shows a sharp rise in temperature after the onset interval - meaning that this is not always the case.

4 Discussion and Future Work

4.1 Short Channel Noise and Background Subtraction

One of the major issues concerning this study is the noise arising from the short channel fluxes. These noise variations are most prevalent at the lows of the solar cycle in the ambient pre-flare phase, where electron contamination dominates the short channel. This can cause the signal after electron noise subtraction to bottom out at negative values, however this becomes less of an issue when the flux starts to increase during the main impulsive phase rise. Pre-flare noise has the largest impact on our background subtraction, which relies on a stream of reliable data in the pre-flare. We flagged up flares that caused the to algorithm fail, which show that B-class flares caused the majority of background algorithm failures - with 9.93% of all B-class flares failing.

The other class of flare that disproportionately caused background failures were of X-class, fail-

ing the algorithm 8.82% of the time. This is caused by 'slow rise' events - predominately associated with larger peak fluxes - which are an issue caused by the NOAA start times. For most events, the NOAA start times give a 'safe', early value for the point in which the flare starts - usually preceding the actual flare start by a few minutes. In these 'slow rise' events, the NOAA start time is calculated part of the way through the impulsive phases rise (as opposed to before). This is caused by flares rising slowly from a level of flux below B1.0, where the start time is only considered to be calculated after it has passed the B1.0 flux threshold. These flares break our assumption about the start time always preceding the actual rise.

For comparison only 2.2% of C-class and 3.4% of M-class events cause the background algorithm to fail, a much smaller proportion. We removed all cases which caused the subtraction algorithm to fail, to limit the overall noise arising from this.

4.2 Interference of the Gradual Phase

Another limitation of our background calculation is that we assume a constant background level during a flare event, however flares that occur during the decay phase of another event will not have a constant background. Despite this, tests made by Ryan et al. (2012) indicate that only 0.7% of events between 1991 and 2007 occur during the decay phase of a previous flare - a negligible amount. However this is more prominent for our study, as if an event occurs during the decay phase of a previous flare then the small SXR contribution from the onset will be 'washed out' by the larger flux contribution - background subtraction may not be as effective in these cases. As none of the flare lists available indicate a good measure for the end of the decay phase of a previous flare, it was decided to 'play it safe' by removing all flares with a NOAA start time that is within 30 minutes of the NOAA end time of a previous flare. This does include the possibility of removing a lot of smaller-class flares from the data set, especially ones that occur during the height of the solar cycle that are more likely to occur in close proximity with short decay phases. This is the most probable reason for a huge 20.5% of flares that were removed due to close proximity. However looking at figure 5, we see that the large M7.3 and X1.1 events have decay phases in excess of thirty minutes - allowing a portion of affected flares to find their way into our final results. A more robust set of filtering - perhaps based on a separate study to better classify the gradual phase of a given flare - likely based on the peak flux of the previous flare could be be used to minimise the needless rejection of suitable events whilst also giving more importance to the longer decay phases of larger flares.

4.3 Limitations of the Ion Chamber Design

The detectors from GOES 1-15 had their limitations, as the X-ray flux was limited to a maxima and minima due to the instrument capability (Chamberlin et al. 2009). During very large flare events (greater than X17.1) the detectors can become over-saturated and thus unable to quantify the true magnitude of the event. The detectors are also able to 'bottom out' which can occur during periods of solar inactivity, where the true X-ray flux is much lower than the limit measured by the detector. The lower cut-off proves to be a major limiting factor due to the electron contamination effects.

Improvements to the XRS were proposed by (Chamberlin et al. 2009) for the next-generation 'GOES-R' satellites of GOES 16-18, and the planned GOES-19. These see the two ion chambers replaced with a quadrant of silicon photodiodes for each bandpass. These diodes are more sensitive to low fluxes and less easily saturayed, so are not as prone to innacuracies. The quadrant of photodiodes can also be used to provide an approximate flare location, allowing for extra analysis of flare location and more accurate background subtraction.

4.4 Numerical Uncertainties

In order to calculate numerical uncertainties on our temperature and emission measure values, we have to propagate errors from our flux values. To determine the uncertainty in raw GOES flux - assuming a Poissonian distribution - we take the square root of the number of counts. In order to get an uncertainty for the background-subtracted flux, σ_{corr}, we must calculate an uncertainty in the background subtraction - which we take to be the standard deviation of the flux bins during that one-minute interval. We combine these uncertainties using the following equation,

$$\sigma_{\mathrm{corr}} = \sqrt{\sigma_{\mathrm{raw}}^2 + \sigma_{\mathrm{backg}}^2}, \tag{7}$$

where σ_{raw} and σ_{backg} are the errors associated with the raw and background fluxes. In order to calculate an average temperature and emission measure, we first calculate a weighted average mean (denoted as subscript 'WM') in the long and the short channels over the onset interval. The error for this value, σ_{WM}, is given by equation 8:

$$\sigma_{\mathrm{WM}} = \sqrt{\frac{\Sigma W \cdot (\phi_{\mathrm{corr}} - \phi_{\mathrm{WM}})^2}{\Sigma W \cdot (N - 1)}}, \tag{8}$$

where W denotes the weights (given by: $W = \frac{1}{\sigma_{\mathrm{corr}}}$), ϕ_{WM} is the weighted-mean flux and N is the number of bins in the sample - which for our fixed one-minute interval will always be equal to 30. We further propagate the error for each channel to obtain an error in the flux ratio,

$$\sigma_{\mathrm{ratio}} = \phi_{\mathrm{ratio}} \cdot \sqrt{\left(\frac{\sigma_{\mathrm{WM},1-8}}{\phi_{\mathrm{WM},1-8}}\right)^2 + \left(\frac{\sigma_{\mathrm{WM},0.5-4}}{\phi_{\mathrm{WM},0.5-4}}\right)^2}, \tag{9}$$

where $\phi_{\mathrm{WM},1-8}$ and $\phi_{\mathrm{WM},0.5-4}$ are the weighted means from each channel, $\sigma_{\mathrm{WM},1-8}$ and $\sigma_{\mathrm{WM},0.5-4}$ are the calculated uncertainties in these means from equation 9. At this point we calculate the temperature by using the response ratio from the bottom-right panel of figure 3. If we assume there is an insignificantly small error associated with these responses, then we can calculate the upper and lower bounds of the temperature from the uncertainty range of the flux ratio. The emission measure errors are similarly calculated by taking the upper and lower limits of temperature and applying to the long channel response curve (red line in top right panel of figure 3). The upper and lower bounds on the long channel response can then be propagated with the uncertainty in the long channel flux average, consistently with equation 5. The percentage errors on the temperature and emission measures from these calculations range from around 5% to 15%. However if we were to assume that the response curves had a 20% uncertainty, then this contribution would dominate and we would see errors at much higher values.

5 Future Work

5.1 Increasing Flare Samples

While the current GOES flare list covers thousands of events of varying strengths, a quick inspection of figure 5 shows that it is not very robust. Many events are able to skip detection by the current algorithms by NOAA, which limits the number of events that are available for analysis. However Plutino et al. (2023) propose a new flare detection method which would increase the number of events detected between 1999 and 2020 from 38,517 to 205,989. The flare-list from this study is currently available, however the authors are still investigating the robustness of their algorithm by looking at statistical properties of flares and comparing with current literature. Once confirmation on the accuracy of this flare list is accepted by the wider field, it is in the best interests of future analysis to apply it to our methods.

We can also expand our data set by searching other GOES satellites when the science quality data in short-cadence measurements becomes available. Currently GOES 8-12 and 16-18 have science-quality data available in 1-minute averages, however these were not precise enough for our investigation so were discarded. Science quality data for these satellites is set to be released in the near future, with the hope that this is also extended to GOES 1-7.

5.2 Hard X-Ray Measurements

We did not use HXR measurements to define the end of the onset interval due to the lack of a consistent HXR data stream. One of the few full-disk HXR satellites in operation during the GOES 13-15 time range is that of RHESSI, however we did not utilise the satellites measurements due to sporadic data coverage, therefore resulting in significant reduction of our sample size. With an improved flare list and science-data availability for short cadence measurements for GOES 8-12, we would have a much larger flare sample from which to try and cross-reference RHESSI and GOES data. This endeavour should be the primary focus on future work into the hot-onset using X-ray measurements, as it would allow a more robust definition of the hot-onset interval and therefore allow a more detailed investigation of its properties.

5.3 Spatial Resolution Measurements

This study has confirmed the existence of the hot-onset sources using 1-D X-ray data. However in order to further investigate the cause of these sources, we may need to utilise alternative data streams such as spatial imaging from AIA/SDO. The AIA takes a 4K full-disk image of the Sun every ten seconds in ten different wavelengths; allowing for inspection of different layers of the solar atmosphere since it is optically thin to different wavelengths. Identification and spatial observation of onset sources would allow for a better determination of the mechanisms that cause the heating of the thermal electrons that give rise to the hot SXR emission of the hot-onset.

6 Conclusion

Hudson et al. (2021) found evidence of 'hot-onset' sources in a sample of four solar flares. These sources are currently unexplained by the standard solar flare model due to the existence of SXR emission before that of HXRs. We conducted a large-scale analysis of the SXR emission of a population of 9,573 flares using two XRS sensors on board GOES-15. Results confirm the work of Hudson et al., with 61.5% of onsets occurring above 10 MK, and 94.7% of onsets occurring over 7 MK. Temperature distributions suggest the prevalence of hot-onset sources occurring in flares of all classes. We note that the onset temperatures are strongly correlated with maximum temperatures and the temperature at the flare peak - indicating a correlation between the heating mechanisms. We have also developed a unique background subtraction algorithm sensitive to low fluxes which with a 95% success rate, unlike alternative methods currently available. Continuation of the work presented here includes widening the sample size of the study when the relevant resources become available, as well as utilising and cross-referencing data from alternative satellites such as SDO/AIA and RHESSI.

References

Archontis, V., & Syntelis, P. 2019, Philosophical transactions. Series A, Mathematical, physical, and engineering sciences, 377, 20180387, doi: 10.1098/rsta.2018.0387

Aschwanden, M. J., Johnson, J. R., & Nurhan, Y. I. 2021, The Astrophysical Journal, 921, 166, doi: 10.3847/1538-4357/ac19a9

Bornmann, P. L. 1990, The Astrophysical Journal, 356, 733, doi: 10.1086/168880

Brown, J. C. 1971, Solar Physics, 18, 489, doi: 10.1007/BF00149070

Brown, J. C., & MacKinnon, A. L. 1985, The Astrophysical Journal, 292, L31, doi: 10.1086/184467

Bruno, A. 2017, Space Weather, 15, 1191, doi: 10.1002/2017SW001672

Chamberlin, P. C., Woods, T. N., Eparvier, F. G., & Jones, A. R. 2009, in SPIE Optical Engineering and Applications, ed. S. Fineschi & J. A. Fennelly, San Diego, CA, 743802. http://proceedings.spiedigitallibrary.org/proceeding.aspx?doi=10.1117/12.826807

Dere, K. P., Landi, E., Mason, H. E., Fossi, B. C. M., & Young, P. R. 1997, Astronomy and Astrophysics Supplement Series, 125, 149, doi: 10.1051/aas:1997368

Dungey, J. W. 1951, PhD thesis, Cambridge University. https://ui.adsabs.harvard.edu/abs/1951PhDT.......23D

Fletcher, L., Dennis, B. R., Hudson, H. S., et al. 2011, Space Science Reviews, 159, 19, doi: 10.1007/s11214-010-9701-8

Garcia, H. A. 1994, Solar Physics, 154, 275, doi: 10.1007/bf00681100

Hannah, I. G., Christe, S., Krucker, S., et al. 2008, The Astrophysical Journal, 677, 704, doi: 10.1086/529012

Hanser, F. A., & Sellers, F. B. 1996, in SPIE's 1996 International Symposium on Optical Science, Engineering, and Instrumentation, ed. E. R. Washwell, Denver, CO, 344–352. http://proceedings.spiedigitallibrary.org/proceeding.aspx?articleid=1021201

Hock, R. A. 2012, PhD Thesis, School of Arts and Sciences, University of Colorado, Boulder, Boulder, CO, USA

Hoven, G. V., & Hurford, G. J. 1986, Advances in Space Research, 6, 83, doi: 10.1016/0273-1177(86)90121-3

Hudson, H. S. 1991, in Bulletin of the American Astronomical Society, Vol. 23, 1064. https://ui.adsabs.harvard.edu/abs/1991BAAS...23R1064H

Hudson, H. S., Simões, P. J. A., Fletcher, L., Hayes, L. A., & Hannah, I. G. 2021, Monthly Notices of the Royal Astronomical Society, 501, 1273, doi: 10.1093/mnras/staa3664

Hurlburt, N., Cheung, M., Schrijver, C., et al. 2012, Solar Physics, 275, 67, doi: 10.1007/s11207-010-9624-2

Lin, R. P., Dennis, B. R., & Benz, A. O., eds. 2003, The Reuven Ramaty High-Energy Solar Spectroscopic Imager (RHESSI): Mission Description and Early Results (Dordrecht: Springer Netherlands), doi: 10.1007/978-94-017-3452-3. http://link.springer.com/10.1007/978-94-017-3452-3

Lin, R. P., & Hudson, H. S. 1976, Solar Physics, 50, 153, doi: 10.1007/BF00206199

Machol, J., Codrescu, S., & Peck, C. 2022a, Readme for GOES-R XRS L2 Data, Tech. rep., National Oceanic Atmospheric Administration

Machol, J., Viereck, R., Peck, C., & III, J. M. 2022b, GOES X-ray Sensor (XRS) Operational Data, Tech. rep., National Oceanic Atmospheric Administration

McTiernan, J. M., Kane, S. R., Loran, J. M., et al. 1993, The Astrophysical Journal, 416, L91, doi: 10.1086/187078

Milligan, R. O., & Ireland, J. 2018, Solar Physics, 293, 18, doi: 10.1007/s11207-017-1233-x

Nagai, F. 1980, Solar Physics, 68, 351, doi: 10.1007/bf00156874

Plutino, N., Berrilli, F., Del Moro, D., & Giovannelli, L. 2023, Advances in Space Research, 71, 2048, doi: 10.1016/j.asr.2022.11.020

Rodriguez, J. V. 2014, GOES EPEAD Science-Quality Electron Fluxes Algorithm Theoretical Basis Document v1.0, Tech. rep., NOAA/NESDIS/NGDC

Ryan, D. F., Milligan, R. O., Gallagher, P. T., et al. 2012, The Astrophysical Journal Supplement Series, 202, 11, doi: 10.1088/0067-0049/202/2/11

Simões, P. J. A., Hudson, H. S., & Fletcher, L. 2015, Solar Physics, 290, 3625, doi: 10.1007/s11207-015-0691-2

Thomas, R. J., Starr, R., & Crannell, C. J. 1985, Solar Physics, 95, 323, doi: 10.1007/BF00152409

Veronig, A. 2003, Hvar Observatory Bulletin, 27, 47

White, S. M., Thomas, R. J., & Schwartz, R. A. 2005, Solar Physics, 227, 231, doi: 10.1007/s11207-005-2445-z

Zanna, G. D., Dere, K. P., Young, P. R., & Landi, E. 2021, The Astrophysical Journal, 909, 38, doi: 10.3847/1538-4357/abd8ce

Zetterlund, E., & Machol, J. 2022, Readme for Science-Quality GOES 13-15 XRS Data, Tech. rep., National Oceanic Atmospheric Administration

Zwaan, C. 1985, Solar Physics, 100, 397, doi: 10.1007/BF00158438